

# Enhanced high-harmonic generation from an all-dielectric metasurface

Hanzhe Liu<sup>1,2\*</sup>, Cheng Guo<sup>3,4</sup>, Giulio Vampa<sup>1</sup>, Jingyuan Linda Zhang<sup>3,4</sup>, Tomas Sarmiento<sup>4,5</sup>, Meng Xiao<sup>4</sup>, Philip H. Bucksbaum<sup>1,2,3,6</sup>, Jelena Vučković<sup>3,4,5</sup>, Shanhui Fan<sup>3,4,5</sup> and David A. Reis<sup>1,3,6\*</sup>

**The recent observation of high-harmonic generation from solids creates a new possibility for engineering fundamental strong-field processes by patterning the solid target with subwavelength nanostructures. All-dielectric metasurfaces exhibit high damage thresholds and strong enhancement of the driving field, making them attractive platforms to control high harmonics and other high-field processes at the nanoscale. Here we report enhanced non-perturbative high-harmonic emission from a Fano-resonant Si metasurface that possesses a classical analogue of electromagnetically induced transparency. The harmonic emission is enhanced by more than two orders of magnitude compared to unpatterned samples. The enhanced high harmonics are highly anisotropic with respect to the excitation polarization and are selective by the excitation wavelength due to its resonant features. By combining nanofabrication technology and ultrafast strong-field physics, our work paves the way for the design of new compact ultrafast photonic devices that operate under high intensities and at short wavelengths.**

High-harmonic generation (HHG) was first reported in rare gas atoms<sup>1</sup>. It is regarded as one of the fundamental processes in strong-field physics and lies at the heart of attosecond photonics<sup>2</sup>. Recently discovered HHG in solids<sup>3–10</sup> provides a new way to investigate novel strong-field photonic applications that cannot be realized in gases. In particular, it opens the possibility of generating and controlling the high harmonics directly from subwavelength nanostructures<sup>11–13</sup>. The effect of nanostructures on solid-state HHG is twofold: first, each individual nanoscale feature interacts with and scatters fundamental light in a non-trivial way depending on its geometry; second, HHG emission profiles in the far field can be controlled by arranging the location of individual nanostructures. For example, harmonics have been generated from Fresnel zone plates producing a diffraction-limited spot in the far field<sup>11</sup>.

One of the challenges in realizing practical devices for ultrafast strong-field nanophotonics is that the nonlinear response for most solids is intrinsically weak, especially when the excitation photon energy is much smaller than the bandgap, which is typically the case in solid-HHG experiments<sup>3–10</sup>. Phase matching in this context is difficult for above-gap harmonics, as the attenuation length for high harmonics is normally much shorter than the coherence length, due to strong absorption during propagation in the bulk<sup>3</sup>. A promising solution is to enhance the driving electric field with nanostructures on a surface<sup>12–18</sup>. Plasmon-enhanced HHG has been reported from metallic antennas deposited on Si<sup>12</sup> and sapphire<sup>13</sup>. However, the

damage threshold of plasmonic-based metal structures is extremely sensitive to the fabrication quality and the high degree of confinement in the vicinity of sharp features, such as edges or corners, significantly limits the overall signal enhancement<sup>12,18,19</sup>.

A dielectric metasurface that hosts an optical resonance provides a promising solution to this issue. Electromagnetically induced transparency (EIT)<sup>20</sup> can give rise to greatly enhanced nonlinear light–matter interactions in the spectral region of the resonance<sup>21</sup>. Enhanced frequency conversion from EIT has been observed in atomic systems<sup>21</sup> and, very recently, enhanced perturbative third-harmonic generation has been reported from photonic devices exhibiting a classical analogue of EIT<sup>14</sup>. In this article, we report enhanced high harmonics from an all-dielectric Si metasurface on a sapphire substrate comprising optically resonant dielectric nanostructures motivated by the work of ref. <sup>14</sup>. We demonstrate that when the metasurface is resonantly excited, the high-harmonic signal is orders of magnitude higher compared to an unpatterned Si film at moderate driving intensities.

## Device working principle

Figure 1 shows an SEM image of the metasurface consisting of a periodic lattice of bar antennas and disk resonators, which is fabricated from a 225-nm-thick single-crystal Si film grown over a 0.53-mm-thick sapphire substrate. It is known that this type of structure hosts a Fano-like resonance, resulting in a classical analogue of EIT<sup>14,22</sup>. The collective oscillations of the electric dipole bar antennas form the ‘bright’ mode, which couple strongly to external excitation with the polarization along the long axis of the bar. The collective oscillations of the magnetic dipole disk resonators form the ‘dark’ mode, which cannot be excited directly by normally incident light, but can couple to the ‘bright’ mode via near-field coupling. The interference of the broadband ‘bright’ mode and narrowband ‘dark’ mode forms a typical three-level Fano-resonant system, as depicted in Fig. 1b, and gives rise to a sharp EIT-like peak in the transmission spectrum<sup>14,22–24</sup>.

We numerically simulate the linear optical properties of the structure as shown in Fig. 1a using commercial software (Lumerical) based on the finite-difference time-domain (FDTD) method (see Methods)<sup>23</sup>. Figure 1c displays the simulated and measured transmission spectrum for our device. An EIT peak is observed in the experiment around 2,320 nm, which agrees well with the simulation. The broadband absorption corresponds to the bright mode of the metasurface while the sharp EIT peak is linked to the excitation of the dark mode of the disk. The central resonant wavelengths

<sup>1</sup>Stanford PULSE Institute, SLAC National Accelerator Laboratory, Menlo Park, CA, USA. <sup>2</sup>Department of Physics, Stanford University, Stanford, CA, USA. <sup>3</sup>Department of Applied Physics, Stanford University, Stanford, CA, USA. <sup>4</sup>E. L. Ginzton Laboratory, Stanford University, Stanford, CA, USA. <sup>5</sup>Department of Electrical Engineering, Stanford University, Stanford, CA, USA. <sup>6</sup>Department of Photon Science, Stanford University, Stanford, CA, USA. \*e-mail: [hanzhe@stanford.edu](mailto:hanzhe@stanford.edu); [dreis@stanford.edu](mailto:dreis@stanford.edu)

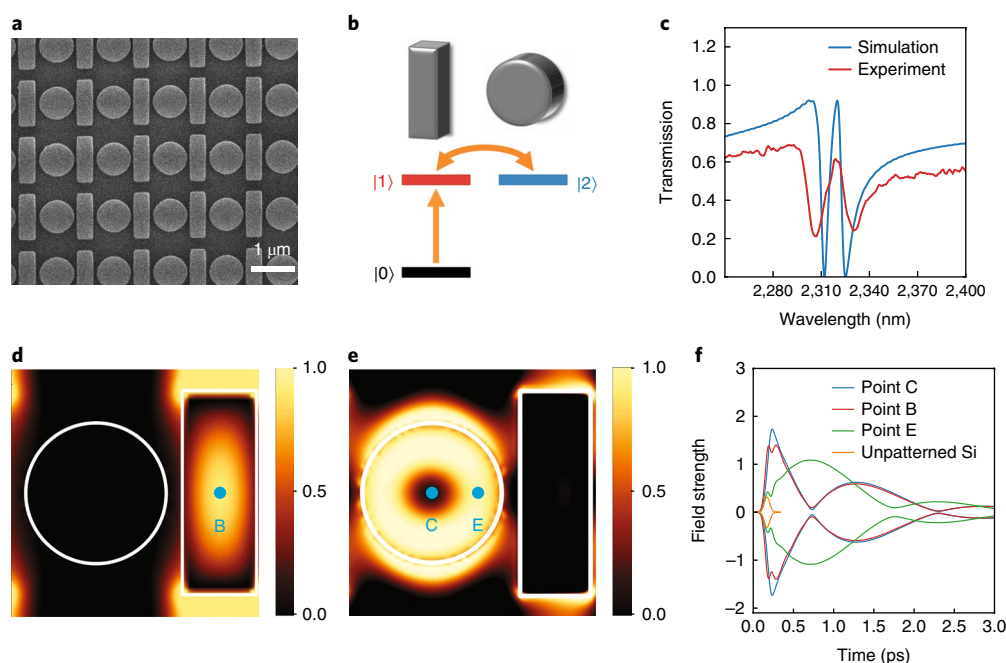


**Fig. 1 | Working principle of the metasurface and resonance characterization.** **a**, An SEM image of the Si metasurface on a sapphire substrate. A single unit cell consists of a dipolar bar antenna and a disk resonator to its right. Geometric parameters of the metasurface are: Si thickness = 225 nm (on top of sapphire); unit cell period = 1,280 nm; length of the bar = 1,022 nm; width of the bar = 347 nm; disk radius = 369 nm; distance from the centre of the bar to the centre of right disk = 652 nm. **b**, Level scheme for the mode coupling in a schematic three-level Fano-resonant system. States  $|1\rangle$  and  $|2\rangle$  correspond to the ‘bright’ mode in the bar and the ‘dark’ mode in the disk. The direct excitation of the ‘bright’ mode is illustrated as  $|0\rangle \rightarrow |1\rangle$ . The near-field coupling between the ‘bright’ mode and the ‘dark’ mode is illustrated as  $|1\rangle \rightarrow |2\rangle \rightarrow |1\rangle$ . **c**, Experimentally measured (red line) and simulated (blue line) transmission spectrum of the metasurface. **d, e**, Mode amplitude for the bar and the disk, respectively. Points B, C, and E denote the bar centre, the disk centre and the disk edge, respectively. **f**, Temporal evolution of the excitation field at the disk centre (point C), the bar centre (point B) and the disk edge (point E) of the structure and from the unpatterned Si film. Field strength is normalized to the peak of the vacuum excitation field.

of the bar mode and the disk modes are numerically determined as 2,318 nm and 2,321 nm, respectively (see Supplementary Information). Figure 1d,e shows the electric field amplitude profiles of the bar mode and disk mode, respectively.

To illustrate the mechanism of HHG enhancement by the metasurface, we simulate the temporal evolution of the electric field in the metasurface and compare it with that in an unpatterned Si film of the same thickness. In each simulation, an identical 59.5 fs linearly polarized plane wave pulse is normally incident on the structure, which is compatible with our experimental condition. The polarization is along the long axis of the bar for the metasurface (see Methods for simulation details). Figure 1f shows the simulated electric field strength as a function of time at three representative points of the metasurface: bar centre (B), disk centre (C) and disk edge (E). All the points are located on the middle plane of the Si layer; the in-plane locations of those points are indicated in Fig. 1d,e. For comparison, Fig. 1f also plots the field evolution on the middle plane of the unpatterned Si film.

The simulation results in Fig. 1f reveal several marked differences between the metasurface and the unpatterned Si film. First, the electric field is greatly enhanced in the metasurface compared to the unpatterned film, due to the excitation of the resonant modes. Here we note that, in the metasurface, the enhanced field extends over a large portion of the active material (Si) (Fig. 1d,e), which is one major difference compared to plasmonic enhancement<sup>12,14</sup>. Second, the temporal duration of field oscillation is significantly extended in the metasurface, due to the high-quality-factor (high-Q) Fano resonance. Both these important features will in general boost the high-harmonic flux.

There are several other features in Fig. 1f that are worth noting. First, the occurrence of the field maximum in the metasurface is

slightly delayed compared to that in the unpatterned film (~64 fs). Second, the field evolution is spatially inhomogeneous. The field envelope at the disk edge, which characterizes the amplitude of the disk dark mode, evolves out of phase with the field envelope at the bar centre, which characterizes the amplitude of the bar mode. This manifests the coupling of the two modes in the time domain (Supplementary Movies show the spatio-temporal evolution of the field in the metasurface for both top and side view of the device). The resonantly enhanced field in the metasurface suggests that the efficiency of extreme nonlinear optical processes can be greatly enhanced at the nanoscale.

### Observation of enhanced high harmonics

We generate solid-state high harmonics using linearly polarized, 1 kHz repetition rate, 70 fs pulses centred at 2,320 nm, which are well below the indirect bandgap of silicon. The laser pulses are focused on the device down to a waist diameter of ~160  $\mu\text{m}$ , covering an area consisting of ~15,600 unit cells of the metasurface. The periodic pattern diffracts the high harmonics. The zeroth-order diffracted harmonics are collected and measured in an ultraviolet–visible spectrometer, and are compared to those emitted from unpatterned regions on the same film under identical illumination and detection conditions.

Figure 2 shows the high-harmonic spectrum produced by the metasurface at an incident excitation intensity of 0.071  $\text{TW cm}^{-2}$ . When the fundamental field is polarized along the bar (red line), odd harmonics from fifth to eleventh are observed, while no harmonics above the fifth are observed in unpatterned Si (dotted black line). At this intensity, the fifth harmonic is enhanced by a factor of 30 compared to the unpatterned film, even though only the zero diffraction order is collected and the total area of structured Si is

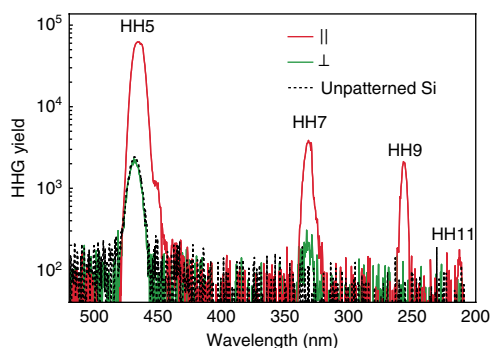


**Fig. 2 | High-harmonic spectra from a Si metasurface.** High-harmonic spectra from fifth to eleventh order when the excitation pulses centred at 2,320 nm are polarized parallel (red line) and perpendicular (green line) to the bar on the metasurface. The dotted black line is the high-harmonic spectrum from the unpatterned Si film. The spectra are taken at a vacuum excitation intensity of  $0.071 \text{ TW cm}^{-2}$ . The reported spectral range is limited by our detection scheme, which cuts off at the short-wavelength edge of the eleventh harmonic.

only 47% of the unpatterned film under the same illumination spot. Not accounting for these two contributions to the high-harmonic flux, we estimate that the lower bound conversion efficiency for the fifth harmonic generated from the metasurface is  $\sim 5 \times 10^{-9}$  at an excitation intensity of  $0.07 \text{ TW cm}^{-2}$  (see Methods). When the polarization of the excitation pulse is perpendicular to the bar (green line), a configuration where the bar dipolar resonance is not excited, only the fifth and seventh harmonics are observed. In this case, the yield for the fifth harmonic is similar to the unpatterned film and a weak seventh harmonic is seen above the noise level, but reduced by a factor of 12 compared to the same harmonic yield in the parallel configuration.

To further determine the HHG enhancement for individual harmonics, we measured the high-harmonic yield as a function of the incident excitation intensity  $I$  (Fig. 3). The polarization of the excitation pulse is parallel to the bars. As illustrated in Fig. 3, all three observable harmonics, fifth, seventh and ninth, show large enhancements in the spectrally integrated yield compared to the unpatterned Si film, especially at relatively low excitation intensities. We note that higher-order harmonics are more enhanced than the low-order harmonics. For instance, the enhancement for the seventh harmonic at around  $0.1 \text{ TW cm}^{-2}$  is more than two orders of magnitude, while the fifth harmonic under same intensity is enhanced by about one order of magnitude.

Solid-state high-harmonic generation is believed to originate from strongly-driven intraband and interband electron dynamics<sup>3–7</sup>. Locally, these dynamics occur at the atomic scale, which is not expected to be altered by the metasurface. Thus, we attribute the enhanced high-harmonic emission to the resonant field enhancement in the nanostructure compared to that in the unpatterned area, consistent with the FDTD simulation. This claim is further supported by the different scaling behaviour of the metasurface-enhanced HHG and HHG from bare Si film. The high-harmonic yield from the metasurface as a function of excitation intensity deviates from the perturbative scaling and exhibits a gradual saturation. Note that the fifth harmonic from bare film is still perturbative ( $I^5$ ) under similar excitation. Saturation of the HHG yield with increasing pump intensity has been seen in previous experiments in the non-perturbative regime<sup>3</sup>. Here we see that after saturation is reached by slowly increasing the driving intensity, the high-harmonic yield does not return to its former value when the intensity is lowered. This suggests that the progressive damage of the structures contributes to the observed saturation (see Supplementary

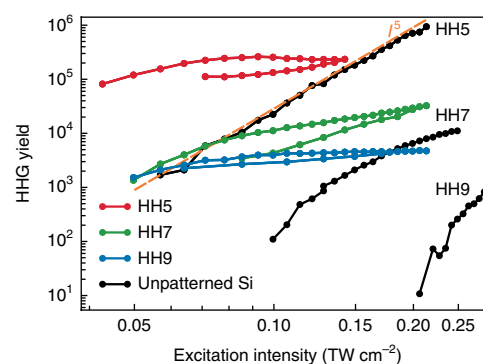


**Fig. 3 | Dependence of non-perturbative high-harmonic yield on excitation intensity.** The measured harmonic yield as a function of vacuum peak excitation intensity  $I$  for the fifth (red), seventh (green) and ninth (blue) harmonic when the excitation pulse centred at 2,320 nm is polarized along the bar. HHG yield is measured as the excitation intensity increases (first) and then decreases when the yield slowly saturates. All harmonics from the metasurface scale non-perturbatively. The black circles show the HHG emission from an unpatterned Si film for the same three harmonic orders. The dashed orange line, which scales as  $I^5$ , is plotted as a guide to the eye.

Information for details). SEM images of damaged metasurfaces (Supplementary Fig. 2) reveal that the damage occurs first at the disks, where simulations predict the highest energy density (Fig. 1f). In addition, the damaged structures in the SEM field of view appear randomly distributed, which is probably due to variation of the field enhancement of individual nanostructures, a result of the small fluctuations in the geometry of each disk and bar induced by the imperfection of the nanofabrication process. Structures with higher field enhancement will damage first when the intensity is gradually increased.

### Wavelength dependence near resonance

To further reveal the resonant nature of the enhanced high harmonics, we measured the high-harmonic spectrum while tuning the central wavelength of the excitation laser pulse through the resonance. Figure 4a–c displays the spectra of the fifth, seventh and ninth harmonics, respectively, as functions of the central wavelength under the same intensity of  $0.1 \text{ TW cm}^{-2}$ . Whereas the 2,326 nm pulse overlaps well with the resonance, the other pulses are detuned away from the EIT peak. At zero detuning, the largest fraction of the excitation pulse spectrum—which is much wider than the width of the resonance—is resonantly coupled to the metasurface, and the harmonics are brightest and their frequencies coincide with odd-integer multiples of the resonance. The effects of detuning on HHG are twofold. First, when the detuning is slight, the harmonic intensity decreases monotonically with increasing detuning of the excitation pulse, because of decreased spectral power overlap between the laser spectrum and the metasurface resonance. This effect has been observed for all three different harmonics. Second, for larger detuning, the fifth-harmonic peak splits (see, for example, the red and purple arrows in Fig. 4a), with one maximum locked to a harmonic of the metasurface resonance and a secondary maximum corresponding to a non-resonant harmonic generation. Only the non-resonant component is measured from the unpatterned film (Fig. 4d). This non-resonant peak is not enhanced since the centre wavelength of the excitation pulse and the metasurface resonance do not overlap. The detailed feature of this observed splitting in the harmonic spectra is the interplay of excitation bandwidth, resonance linewidth, enhancement factor and pump intensity. Since the data are taken at a relatively low vacuum excitation intensity on the metasurface where the non-resonant excitation is not strong

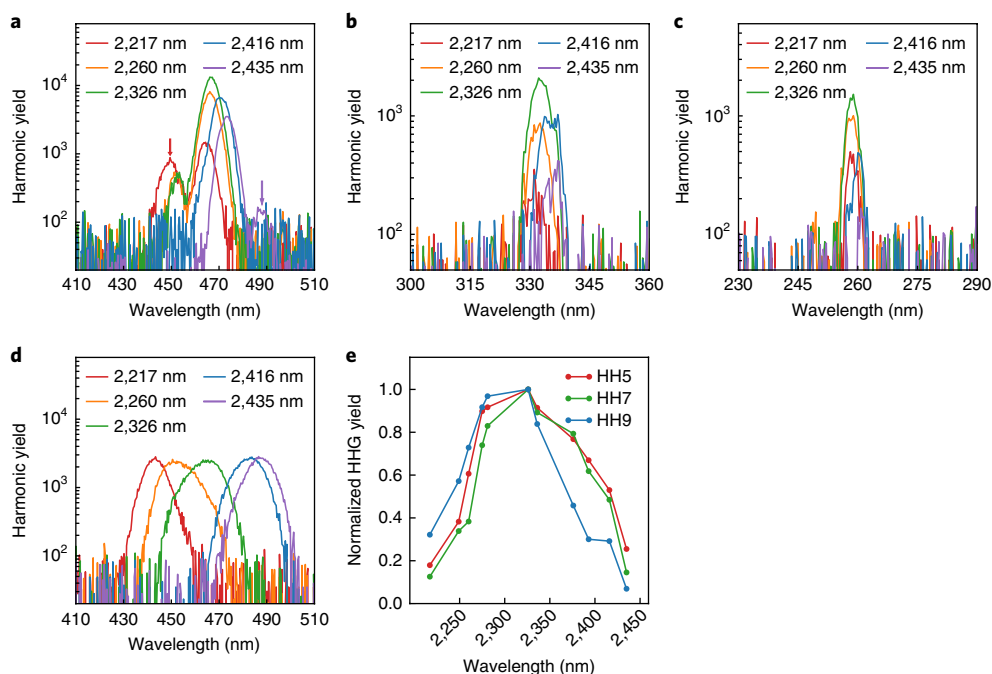


**Fig. 4 | Dependence of the high-harmonic spectra on the excitation wavelength.** **a**, Fifth-harmonic spectrum from the metasurface under excitation at 2,217 nm, 2,260 nm, 2,326 nm, 2,416 nm and 2,435 nm. 2,326 nm is resonant with the EIT peak. The red and purple arrows denote the splitting of the harmonic spectra. **b**, **c**, Spectra for the seventh and ninth harmonics, respectively, under the same pump wavelength as in **a**. **d**, Fifth-harmonic spectrum from an unpatterned Si film under the same excitation wavelength, but for a higher intensity of  $0.22 \text{ TW cm}^{-2}$ . **e**, Integrated fifth- (red dots), seventh- (green dots) and ninth-harmonic (blue dots) yield as a function of excitation wavelength.

enough to generate seventh and ninth harmonics outside the resonance, no splitting for the seventh and ninth orders is observed. Figure 4e shows that the spectrally integrated HHG yield decreases as the excitation laser is detuned from resonance.

## Discussion and outlook

Our demonstration of enhanced HHG on an all-dielectric metasurface has several important implications.

First, compared to plasmonic nanostructures, an all-dielectric metasurface has the advantage of high transparency for the fundamental pulse and potentially higher damage threshold as a high-harmonic source. It has been reported<sup>25</sup> that under a 15 fs pulse centred at 825 nm excitation, gold nano-antennas will melt and subsequently change their shape dramatically at an incident intensity of a few  $10^{11} \text{ W cm}^{-2}$ . Dielectric materials with larger bandgap, have been reported<sup>4,10</sup> to survive up to  $10^{13} \text{ W cm}^{-2}$ , which is crucial for the XUV HHG process in solids, where the excitation intensity is normally one order of magnitude higher than the excitation intensity reported in current work<sup>4,8,10</sup>. One way to push the high-energy cutoff into the XUV regime might be to replace the Si metasurface with a larger bandgap material, known to generate VUV/XUV harmonics (for example,  $\text{SiO}_2$ <sup>4,26</sup>,  $\text{ZnO}$ <sup>3</sup>,  $\text{MgO}$ <sup>10</sup>), and to be robust under higher excitation intensity.

Second, unlike most plasmonic-based nanostructures, dielectric photonic structures can exhibit sharp resonances<sup>14–17,22,27–31</sup> that are narrower than the bandwidth of the typical excitation pulses used in solid HHG experiments<sup>3–10</sup>. For instance, dielectric photonic crystals with quality factors of a few thousand can be routinely designed and fabricated<sup>32</sup>. This opens a novel avenue to control the HHG process in both the temporal and the frequency domains. A high-Q resonance in the frequency domain is equivalent to a long lifetime of confinement of the excitation field in the device, which can in principle lead to a high-harmonic spectrum with narrowed linewidth and, equivalently, longer coherence time and longer temporal

duration, tunable by adjusting the Q of the device. Furthermore, when an optically resonant metasurface is excited with a broadband transform-limited input pulse, destructive interference may be induced between different spectral components near the resonant wavelength, limiting the overall peak transient energy coupled into the metasurface<sup>33</sup>. By coherent control of the input pulse, especially by tuning the spectral phase via pulse shaping techniques, one can control the peak field coupled into the dielectric nanostructure and, in this case, further increase the extreme nonlinear light–matter interaction strength.

Third, the polarization state of light can be controlled by rearranging the position of individual nanoresonators in an all-dielectric metasurface<sup>29,30,34,35</sup>. In general, control of both the amplitude and phase of the infrared excitation light is possible with anisotropic nanostructures that are rotated periodically<sup>29,30,34,35</sup>. This degree of control is transferred to the high harmonics, thereby enabling spatial manipulation of high-harmonic emission to generate arbitrary polarization states as well as non-zero orbital angular momentum<sup>36</sup>.

## Methods

Methods, including statements of data availability and any associated accession codes and references, are available at <https://doi.org/10.1038/s41567-018-0233-6>.

Received: 14 November 2017; Accepted: 27 June 2018;

Published online: 6 August 2018

## References

1. Ferray, M. et al. Multiple-harmonic conversion of 1064 nm radiation in rare gases. *J. Phys. B* **21**, L31–L35 (1988).
2. Vampa, G., Fattahi, H., Vucković, J. & Krausz, F. Nonlinear optics: Attosecond nanophotonics. *Nat. Photon.* **11**, 210–212 (2017).
3. Ghimire, S. et al. Observation of high-order harmonic generation in a bulk crystal. *Nat. Phys.* **7**, 138–141 (2011).



4. Luu, T. T. et al. Extreme ultraviolet high-harmonic spectroscopy of solids. *Nature* **521**, 498–502 (2015).
5. Vampa, G. et al. Linking high harmonics from gases and solids. *Nature* **522**, 462–464 (2015).
6. Hohenleutner, M. et al. Real-time observation of interfering crystal electrons in high-harmonic generation. *Nature* **523**, 572–575 (2015).
7. Schubert, O. et al. Sub-cycle control of terahertz high-harmonic generation by dynamical Bloch oscillations. *Nat. Photon.* **8**, 119–123 (2014).
8. Ndabashimiye, G. et al. Solid-state harmonics beyond the atomic limit. *Nature* **534**, 520–523 (2016).
9. Liu, H. et al. High-harmonic generation from an atomically thin semiconductor. *Nat. Phys.* **13**, 262–265 (2016).
10. You, Y. S., Reis, D. A. & Ghimire, S. Anisotropic high-harmonic generation in bulk crystals. *Nat. Phys.* **13**, 345–349 (2017).
11. Sivilis, M. et al. Tailored semiconductors for high-harmonic optoelectronics. *Science* **357**, 303–306 (2017).
12. Vampa, G. et al. Plasmon-enhanced high-harmonic generation from silicon. *Nat. Phys.* **13**, 659–662 (2017).
13. Han, S. et al. High-harmonic generation by field enhanced femtosecond pulses in metal–sapphire nanostructure. *Nat. Commun.* **7**, 13105 (2016).
14. Yang, Y. et al. Nonlinear Fano-resonant dielectric metasurfaces. *Nano Lett.* **15**, 7388–7393 (2015).
15. Liu, S. et al. Resonantly enhanced second-harmonic generation using III–V semiconductor all-dielectric metasurfaces. *Nano Lett.* **16**, 5426–5432 (2016).
16. Shcherbakov, M. R. et al. Enhanced third-harmonic generation in silicon nanoparticles driven by magnetic response. *Nano Lett.* **14**, 6488–6492 (2014).
17. Grinblat, G., Li, Y., Nielsen, M. P., Oulton, R. F. & Maier, S. A. Enhanced third harmonic generation in single germanium nanodisks excited at the anapole mode. *Nano Lett.* **16**, 4635–4640 (2016).
18. Stockman, M. I. Nanoplasmonics: The physics behind the applications. *Phys. Today* **64**, 39–44 (February, 2011).
19. Gramotnev, D. K. & Bozhevolnyi, S. I. Plasmonics beyond the diffraction limit. *Nat. Photon.* **4**, 83–91 (2010).
20. Boller, K., Imamolu, A. & Harris, S. Observation of electromagnetically induced transparency. *Phys. Rev. Lett.* **66**, 2593–2596 (1991).
21. Fleischhauer, M., Imamoglu, A. & Marangos, J. P. Electromagnetically induced transparency: Optics in coherent media. *Rev. Mod. Phys.* **77**, 633–673 (2005).
22. Yang, Y., Kravchenko, I. I., Briggs, D. P. & Valentine, J. All-dielectric metasurface analogue of electromagnetically induced transparency. *Nat. Commun.* **5**, 5753 (2014).
23. Zhang, S., Genov, D. A., Wang, Y., Liu, M. & Zhang, X. Plasmon-induced transparency in metamaterials. *Phys. Rev. Lett.* **101**, 047401 (2008).
24. Liu, N., Hentschel, M., Weiss, T., Alivisatos, A. P. & Giessen, H. Three-dimensional plasmon rulers. *Science* **332**, 1407–1410 (2011).
25. Pfullmann, N. et al. Nano-antenna-assisted harmonic generation. *Appl. Phys. B* **113**, 75–79 (2013).
26. You, Y. S. et al. High-harmonic generation in amorphous solids. *Nat. Commun.* **8**, 724 (2017).
27. Krasnok, A., Tymchenko, M. & Alù, A. Nonlinear metasurfaces: A paradigm shift in nonlinear optics. *Mater. Today* **21**, 8–21 (2017).
28. Kuznetsov, A. I., Miroshnichenko, A. E., Brongersma, M. L., Kivshar, Y. S. & Luk'yanchuk, B. Optically resonant dielectric nanostructures. *Science* **354**, aag2472 (2016).
29. Li, G., Zhang, S. & Zentgraf, T. Nonlinear photonic metasurfaces. *Nat. Rev. Mater.* **2**, 17010 (2017).
30. Jahani, S. & Jacob, Z. All-dielectric metamaterials. *Nat. Nanotech.* **11**, 23–36 (2016).
31. Limonov, M. F., Rybin, M. V., Poddubny, A. N. & Kivshar, Y. S. Fano resonances in photonics. *Nat. Photon.* **11**, 543–554 (2017).
32. Khitrova, G., Gibbs, H. M., Kira, M., Koch, S. W. & Scherer, A. Vacuum Rabi splitting in semiconductors. *Nat. Phys.* **2**, 81–90 (2006).
33. Sandhu, S., Povinelli, M. L. & Fan, S. Enhancing optical switching with coherent control. *Appl. Phys. Lett.* **96**, 3–5 (2010).
34. Li, G. et al. Continuous control of the nonlinearity phase for harmonic generations. *Nat. Mater.* **14**, 607–612 (2015).
35. Yu, N. & Capasso, F. Flat optics with designer metasurfaces. *Nat. Mater.* **13**, 139–150 (2014).
36. Devlin, R. C., Ambrosio, A., Rubin, N. A., Mueller, J. P. B. & Capasso, F. Arbitrary spin-to-orbital angular momentum conversion of light. *Science* **358**, 896–901 (2017).

## Acknowledgements

This project was supported primarily by the Air Force Office of Scientific Research under grant no. FA9550-14-1-0108. We thank S.Ghimire and J.Lu for technical support.

## Author Contributions

H.L. and C.G. contributed equally to this work. H.L. conceived the experiment. C.G. and M.X. performed FDTD simulations. H.L. and J.L.Z. fabricated the device. H.L. and G.V. performed the HHG measurement under the supervision of D.A.R. H.L., C.G., T.S., and J.L.Z. characterized the resonance. All authors contributed to the discussion and preparation of the manuscript.

## Competing interests

The authors declare no competing interests.

## Additional information

**Supplementary information** is available for this paper at <https://doi.org/10.1038/s41567-018-0233-6>.

**Reprints and permissions information** is available at [www.nature.com/reprints](http://www.nature.com/reprints).

**Correspondence and requests for materials** should be addressed to H.L. or D.A.R.

**Publisher's note:** Springer Nature remains neutral with regard to jurisdictional claims in published maps and institutional affiliations.

## Methods

**Device simulation.** The numerical results presented in Fig. 1c–f are calculated using Lumerical FDTD Solutions with periodic boundary conditions along the in-plane directions for each unit cell and PML boundary conditions  $3\text{ }\mu\text{m}$  above and  $5\text{ }\mu\text{m}$  below the metasurface plane. The geometry parameters used in the simulation are as indicated in the caption of Fig. 1a. A plane-wave pulse source, linearly polarized along the long axis of the bar, is normally incident on the structure from the air side. The wavelength of the pulse source is set as  $2.25\text{--}2.40\text{ }\mu\text{m}$ ; in the time domain, this corresponds to a pulse with a duration of  $59.5\text{ fs}$ , a centre frequency of  $129\text{ THz}$  and a bandwidth of  $8.33\text{ THz}$ . The total simulation time is  $20,000\text{ fs}$  with a time step of  $0.068\text{ fs}$ . The mode profiles in Fig. 1d,e are determined using frequency profile monitors in Lumerical FDTD. The monitor for the disk (bar) mode is set to the wavelength of  $2.32(2.38)\text{ }\mu\text{m}$  and uses the time apodization feature to extract the field profile at that wavelength using Fourier transforms. Two movies that show the spatio-temporal evolution of the fields for top and side views of a single unit cell of the metasurface, respectively, are included in the Supplementary Information.

**Device fabrication.** The devices were fabricated using a Si-on-sapphire wafer, with a nominal  $225\text{-nm}$ -thick device layer and  $530\text{-}\mu\text{m}$ -thick substrate. A JEOL JBX-6300FS electron-beam lithography system was used to pattern a  $320\text{-nm}$ -thick AR-P 6200.09 electron-beam resist layer spun on Si surface. A plasma etcher was used to transfer the pattern and etch through Si with  $\text{BCl}_3/\text{Cl}_2/\text{O}_2$  chemistry.

The resist mask was then stripped via oxygen plasma and the device was cleaned in piranha solution.

**Measurement of high harmonics.** To generate high harmonics, the idler beam of a Ti:sapphire laser-pumped optical parametric amplifier (OPA), operating at a  $1\text{ kHz}$  repetition rate, is used to excite the sample at normal incidence. The centre wavelength of the idler is tuned around  $2.3\text{ }\mu\text{m}$  and the time duration is around  $70\text{ fs}$ . HHG is collected and measured in the transmission geometry with an ultraviolet–visible spectrometer after the sample. To reduce the scattering inside the spectrometer, an ultraviolet-grade fused silica prism is placed before the spectrometer to pre-disperse the HHG signal. The reported high-harmonic spectral range is limited by the short-wavelength cutoff of the spectrometer. The spectrometer and detector response is calibrated at a single wavelength near the fifth harmonic. A lower limit of the conversion efficiency for the fifth harmonic is estimated to be around  $5 \times 10^{-9}$  from the metasurface at an excitation intensity of  $0.07\text{ TW cm}^{-2}$ . Note that in this lower-bound estimation only the zeroth-order diffraction of the fifth harmonic is considered and the absorption loss from the optics is not taken into account.

**Data availability.** The data that support the plots within this paper and other findings of this study are available from the corresponding author upon reasonable request.